Ongoing Fixed Wing Research within the NASA Langley Aeroelasticity Branch

Robert Bartels[1], Pawel Chwalowski[1], Christie Funk[2], Jennifer Heeg[1], Jiyoung Hur[3], Mark Sanetrik[1], Robert Scott[4],
Walter Silva[4], Bret Stanford[2], Carol Wieseman[4]
NASA Langley Research Center, Hampton, VA, 23681

The NASA Langley Aeroelasticity Branch is involved in a number of research programs related to fixed wing aeroelasticity and aeroservoelasticity. These ongoing efforts are summarized here, and include aeroelastic tailoring of subsonic transport wing structures, experimental and numerical assessment of truss-braced wing flutter and limit cycle oscillations, and numerical modeling of high speed civil transport configurations. Efforts devoted to verification, validation, and uncertainty quantification of aeroelastic physics in a workshop setting are also discussed. The feasibility of certain future civil transport configurations will depend on the ability to understand and control complex aeroelastic phenomena, a goal that the Aeroelasticity Branch is well-positioned to contribute through these programs.

Nomenclature

AePW	Aeroelastic Prediction Workshop
AoA	angle of attack
ASE	aeroservoelastic
BSCW	Benchmark Supercritical Wing
CFD	computational fluid dynamics
CRM	Common Research Model
DMCS	distributed multiple control surfaces
EBF^3	electron beam freeform fabrication
FEM	finite element method
FGM	functionally graded materials
FRF	frequency response function
FUN3D	unstructured CFD software developed at NASA LaRC
GVT	ground vibration test
LCO	limit cycle oscillation
LES	large eddy simulation
OTT	oscillating turntable
PAPA	pitch and plunge apparatus
RANS	Reynolds-averaged Navier-Stokes
ROM	reduced order model
SUGAR	Subsonic Ultra Green Aircraft Research
TBW	truss-braced wing
TDT	Transonic Dynamics Tunnel
ZONA51	oscillatory supersonic lifting surface theory

---

[1] Aerospace Engineer, Aeroelasticity Branch, AIAA Senior Member.
[2] Research Aerospace Engineer, Aeroelasticity Branch, AIAA Member.
[3] Senior Aeronautical Engineer, Analytical Mechanics Associates Inc.
[4] Aerospace Engineer, Aeroelasticity Branch, AIAA Associate Fellow.

I. Introduction

The purpose of this article is to summarize ongoing research efforts within the Aeroelasticity Branch at the NASA Langley Research Center. Though the branch has historically been (and is currently) involved in a wide range of research topics of interest to NASA in particular and the aerospace community in general [1][2][3][4], including space applications [5] and rotorcraft [6][7], the focus of this paper is on recent progress in computational analysis, experimental testing, and design optimization of fixed wing aircraft. The work summarized here is done in close collaboration with academia, industry, and other government laboratories, and is largely concerned with the development of the next generation of civil transport aircraft. Historically, many branch contributions have furthered the general understanding of various aeroelastic [1] and aeroservoelastic [2] phenomena. It is likewise expected that each of the ongoing research programs described here will both contribute to, and extend, the state-of-the-art for fixed wing aeroelasticity/aeroservoelasticity.

Four research programs will be summarized in this paper. Two are concerned with the aeroelastic behavior of subsonic transports, one with supersonic transports, and a fourth project is more generally concerned with the validation, verification, and uncertainty quantification of modern computational aeroelasticity tools via a workshop setting. For the subsonic transport research, planned generational aircraft efficiency improvements will require high-aspect-ratio wings that are very lightweight, flexible, and potentially structurally non-traditional in configuration. These factors, to a greater extent than found with the current generation of transports, place a strong onus upon understanding and controlling the resultant aeroelastic and aeroservoelastic behavior. Many of the same overall issues define the supersonic transport work described here, though few aircraft exist which can be used to baseline the computed and measured aeroelastic performance.

Much of the work described here, for all four research programs, skews towards the transonic flight range. This is partially due to the branch's long term relationship with the Transonic Dynamics Tunnel (TDT) [3][4] and partially due to the inherently complex and critical nature of the flow physics in this regime. Transonic aeroelastic problems are typified by strong nonlinearities, unsteady effects, and multidisciplinary couplings, each of which complicate the numerical analysis, experimental testing, and validation/comparison efforts between the analysis and testing. All of the research topics discussed here are driven by programs whose overall success hinges, to some degree, on the ability to harness these highly complex aeroelastic issues for the next generation of civil transport aircraft wings.

Ongoing research described in this paper (and graphically reviewed in Figure 1) is summarized as follows:

1. Aeroelastic tailoring and optimization of subsonic transport wing structures (Figure 1a, Section II): this work utilizes formal numerical aerostructural optimization for targeted reduction in structural weight and/or fuel burn. The work is specifically interested in non-traditional aeroelastic tailoring methods, such as functionally graded materials, tow steered composite laminates, curvilinear ribs/spars/stringers, and topologically-optimized structures.

2. Wind tunnel testing of a truss-braced wing (Figure 1b, Section III): a truss-braced wing (TBW) configuration can enable higher wing spans compared to conventional cantilevered configurations, but the complex aeroelastic flutter and limit cycle oscillation mechanisms of the TBW require further study. An aeroelastically-scaled wind tunnel TBW model was designed and fabricated, and aeroservoelastic (ASE) wind tunnel testing in the TDT was completed in April 2014. Test program goals included the identification of open- and closed-loop flutter boundaries, as well as gust load alleviation.

3. Computational modeling of a truss-braced wing (Figure 1c, Section IV): this effort is a numerical accompaniment to the experimental TDT testing described above. A beam-rod finite element model of the test article, developed and tuned to existing ground vibration test (GVT) data, is coupled to both a linear doublet lattice method and a computational fluid dynamics (CFD) code via various splining tools. Transonic flutter boundaries, flutter mechanisms, and limit cycle oscillation onset boundaries are computed across a range of angles of attack, geometric structural nonlinearities, and CFD grid densities, for comparison with TDT data.

4. Numerical modeling of a low-boom supersonic configuration (Figure 1d, Section V): this research program studies the aeroelastic and aeroservoelastic behavior of a supersonic transport configuration developed by Lockheed-Martin. The slender configuration of the aircraft results in unique couplings between the wing vibration and the rigid body flight dynamics, as well as with the engine propulsion characteristics. Design metrics mirror many of those of interest for the subsonic configuration work, with the obvious addition of a low-boom requirement. Reduced order models can also be used to obtain greater insight into the flutter mechanisms (via root locus plots typically unavailable with CFD-based tools) at a lower computational cost.

5. Aeroelastic Prediction Workshop (Figure 1e, Section VI): this final project is not driven by any specific aircraft configuration, but more broadly concerned with issues related to the current state-of-the art of aeroelastic predictive capability via validation with existing data sets. Twenty-four analysis teams from ten nations compared results from their own analysis codes in the first workshop, AePW-1, which concentrated on the analysis of the unsteady flow phenomena with some weak coupling between aerodynamics and the structure. The planned AePW-2 builds on the experiences of the AePW-1 workshop and extends the benchmarking effort to aeroelastic flutter solutions.
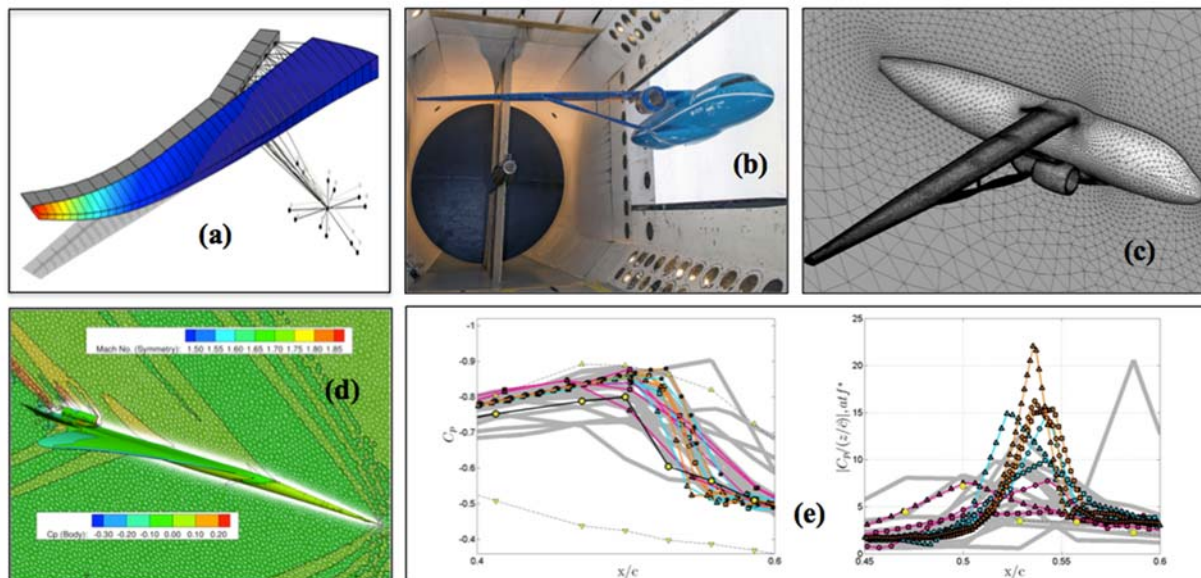
Figure 1. Overview of ongoing aeroelastic fixed wing research in the Aeroelasticity Branch: (a) aeroelastic tailoring of subsonic cantilever wings, (b) TDT testing of a truss-braced wing, (c) numerical modeling of a truss-braced wing, (d) numerical modeling of a low-boom supersonic configuration, (e) the Aeroelastic Prediction Workshop.

II. Aeroelastic Tailoring of Subsonic Transport Wing Structures

The configuration studied in this research program is the conceptual Common Research Model (CRM) [8]. This configuration, which is meant to emulate a single-aisle commercial transport aircraft wing, has an aspect ratio of 9, a leading-edge sweep angle of 35°, and a cruise Mach number of 0.85. The outer mold line [8] is populated with a conventional wingbox of upper and lower skins, a leading- and trailing-edge spar, ribs, and stringers. Aeroelastic optimization is then conducted on this finite element wing structure, with the goal (objective function) to minimize structural mass under stress and panel buckling constraints spread across several trimmed static aeroelastic maneuver loads, and dynamic flutter constraints. This research program is particularly interested in understanding how novel and non-traditional structural configurations (e.g., design techniques recently enabled by improvements in materials and manufacturing) can provide aeroelastically feasible mass reductions over conventional wing structures.

A. Aeroelastic Tailoring
Three different types of design variables are considered. The first tailors the stiffness and mass distribution throughout the shell structures in the wingbox [9]. This is most predominately done in the wing skins, as these structures bear the majority of the aeroelastic load, but can be done in the ribs, spars, and stringers as well. One idea to enable such an aeroelastically-tailored structure is to use additive manufacturing techniques (such as electron beam freeform fabrication (EBF[3]) [10]) to manufacture the wing structures. One example of this is given in Figure 2: the top left picture shows a situation where the CRM wing skin is discretized into panels, and the thickness of each panel is optimized (minimize mass of the structure subject to aeroelastic constraints). This follows standard practices for current aircraft structures [11]. Alternatively, the optimizer can be allowed to tailor finely detailed spatial variations in thickness, shown on the bottom left of Figure 2. Localized continuous undulations in thickness

are evident across adjacent panels, likely driven by panel buckling mechanics. Although the peak thickness in this structure is higher than seen in the discrete structure, it weighs 8% less, as the design space has been greatly expanded. The additive manufacturing cost to build a wing skin with a continuously varying thickness profile may be higher, however, potentially counteracting the aeroelastic benefits.
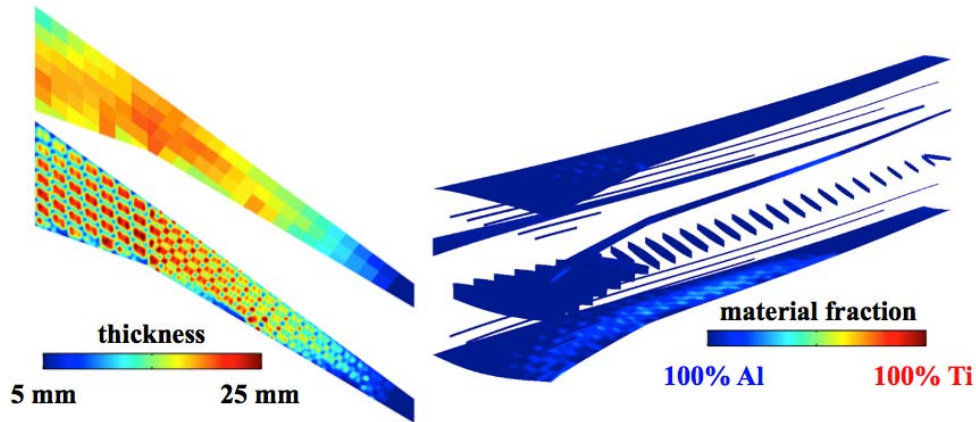

Figure 2. Optimal CRM wingbox structures using additive manufacturing: localized shell thickness variations (left), and functionally graded metals (right).

Another example of using additive manufacturing for aeroelastic tailoring is to use functionally graded metals (FGM), as shown on the right side of Figure 2. This is a situation where the material properties of a metallic structure may be spatially blended between two extremes (material A and B) [12]. The case of aluminum and titanium is particularly interesting. The former material is commonly utilized for subsonic transports, whereas titanium is not, due to its excessive density. However, an optimizer may be able to find a good balance between this weight penalty and the beneficial improvements in stiffness that titanium provide. Such a result is shown on the right side of Figure 2: 100% titanium is not selected by the optimizer anywhere (as this would be too heavy, and mass minimization is the ultimate goal of the optimization), but between a 20-80 and 30-70 titanium-aluminum mix is utilized throughout the lower skins. This result is 4% lighter than a comparable optimization study that only utilizes aluminum structures. The added stiffness of the titanium allows the optimizer to remove structural material elsewhere (through thickness design variables that are not shown), and this weight reduction completely offsets the added weight of the titanium.

Composite structures offer another method to tailor the stiffness and mass distribution throughout the shell structures in the wingbox. While laminated wing structures are well within current aircraft design practices [11], automated fiber tow placement machines can now lay laminate fibers along precise curvilinear paths [13]. Tow steering may provide a laminate analogue to the localized metallic thickness variations discussed above. For this research effort, composite laminates are only considered in the skins. The details of the stacking sequence are optimized for each skin panel (limited to only 0°, ±45°, and 90° ply angles), and a single steering curve, continuously varying from root to tip, is optimized as well. Each stacking sequence is rotated in its entirety based on the local steering angle, and the steering path is optimized via control points at each rib. A typical optimal steering path result is shown in Figure 3; the related optimal stacking sequences for each panel are not shown. As above, optimization entails mass minimization under trimmed static aeroelastic constraints (stress, buckling), and flutter constraints.

Both local and global steering trends are seen in Figure 3, where local steering undulations are likely due to panel buckling, much like the lower left thickness tailoring result of Figure 2. Steering curves with large curvature across multiple panels (global trends) are driven by bend-twist coupling for static aeroelastic load alleviation, flutter mitigation, etc. Relative to an optimization study that only considers straight fibers within each panel, the steered result of Figure 3 weighs 6% less. Further improvements may be obtained if each layer of each laminate was steered independently (which may be done using modern fiber placement technologies [13]), but this would provide laminates that are composed of fiber angles beyond the traditional 0°, ±45°, and 90° choices, leading to certification concerns [11].
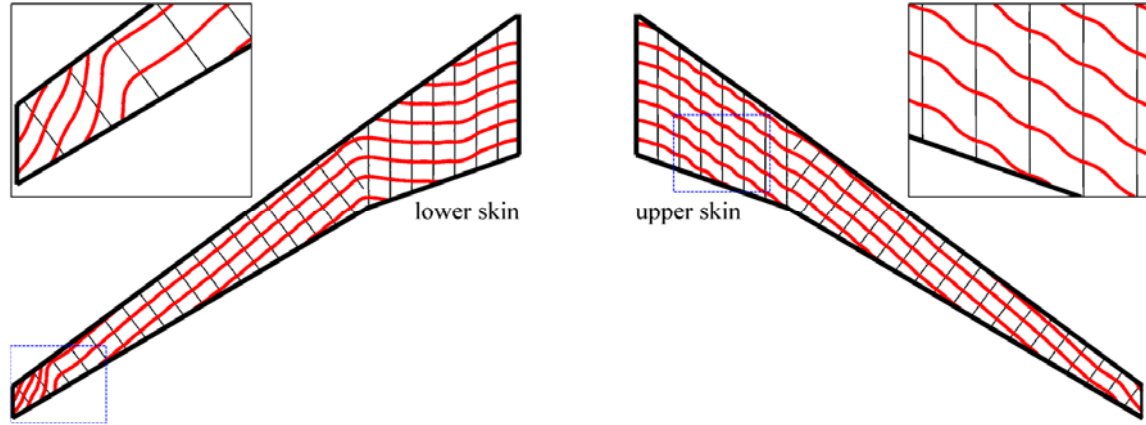
Figure 3. Optimal tow-steered fiber paths for the composite CRM wing skins.

B. Aeroelastic Topology Optimization

The results of Figure 2 and Figure 3 were conducted with a fixed rib-spar-stringer layout within the wingbox, and optimization identifies the best distribution of stiffness and mass along these shell members. The second type of design variable studied in this research program relaxes this constraint, and looks at topology optimization. A graphical summary of ongoing topology optimization activities is given in Figure 4. First, one may parameterize and optimize the number, orientation, spacing, and curvature of the ribs, spars, and stringers within the wingbox, as seen in the upper left of Figure 4. This utilizes the SpaRibs concept [14]: curved/oriented spars and ribs blur the traditionally disparate roles these structures play towards tailoring load paths. This type of topology optimization is difficult to solve, due to the discrete nature of some of the design variables (i.e., the number of ribs), and also due to the fact that, for each new design, the structural geometry and the meshing are reconstructed from scratch. Either of these processes may fail, leaving a gap in the design space. Despite these issues, it is important to understand the size of the aeroelastically-feasible weight reductions enabled by the use of curvilinear design variables, and whether these weight reductions offset the increased manufacturing costs.
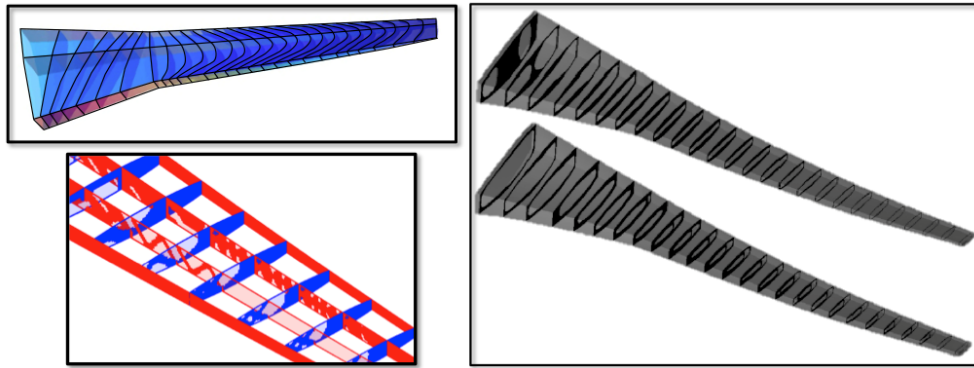
Figure 4. Summary of aeroelastic topology optimization research.

The lower left of Figure 4 considers the optimal topology of lightening holes within rib and spar structures [15]. Ideally, the original rib-spar layout for this exercise would come from an optimal SpaRib result; the layout in the figure is simply a standard orthogonal layout. This result, which is zoomed-in at a point mid-way between the wing root and tip, shows a number of finely-detailed topological features (cross-bracing, cut-outs, etc.) driven by aeroelastic physics. The result in Figure 4 utilizes two internal spars (in addition to the leading and trailing spars), though a true transport wingbox of this size probably wouldn't use any internal spars [11]. Future work will need to add far more internal spars. Expanding the design space in this way will allow the optimizer to place partial span full-depth spars (or cross-bracing) wherever it wants within the wingbox, and then hollow out the rest, leaving behind stringers.

The final topology optimization concept under consideration (right side of Figure 4) abandons the rib-spar concept entirely, and instead fills the wingbox with some optimal three-dimensional distribution of material [16]. This is done by discretizing the box with brick finite elements and assigning a binary design variable to each element: (0) void or (1) solid. The preliminary results in the figure are topologies obtained under various aeroelastic load cases. Slices (not ribs, as pre-defined ribs are not utilized here) are shown of the three-dimensional topology. Though some partial-span full-depth spars are formed, the optimizer is mostly concerned with tailoring the upper and lower skin thickness. The lack of commonality with conventional rib-spar orthogonal layouts is likely due to the exclusion of skin buckling metrics. Rib structures have little impact on the load paths through a wing, but their spacing dictates panel size, and panel size defines buckling resistance. Inclusion of skin buckling constraints is currently under investigation.

C. Distributed Multiple Control Surfaces

The final type of design variable considered for aeroelastic tailoring is scheduling the quasi-static and dynamic deflections of control surfaces along the trailing-edge. Optimizing the static and dynamic deflections of these control surfaces would change the *apparent* stiffness and mass of the wing structure, rather than the true quantities, but these divisions are blurred in any case, due to the coupled nature of an aeroelastic system. Simultaneously designing the wing structure and the actuator deflections will allow an optimizer to take advantage of the synergies between the structural and actuator design variables.

Distributed multiple control surfaces (DMCS) may be used in two distinct ways. First, their deflection patterns may be scheduled in a quasi-steady manner for maneuver load alleviation. A separate deflection pattern may be optimized for each trim load case, where the distributed control surfaces would simultaneously alleviate the loads into the wing structure and help maintain aerodynamic trim. An example of this is seen in Figure 5. Structural design variables are optimized concurrently (though not shown in the figure) for weight reduction. Material can be removed in a feasible manner, as the DMCS system has alleviated the loads into the structure. The control surfaces may also be used for active flutter mitigation or gust rejection, where each flap dynamically oscillates about the steady-state position found with the methods in the previous paragraph (superposition). This introduces a 3rd type of design variable into the aeroelastic optimization, i.e., the details of the controller. Recent aeroservoelastic optimization results may be found in Ref. [17].
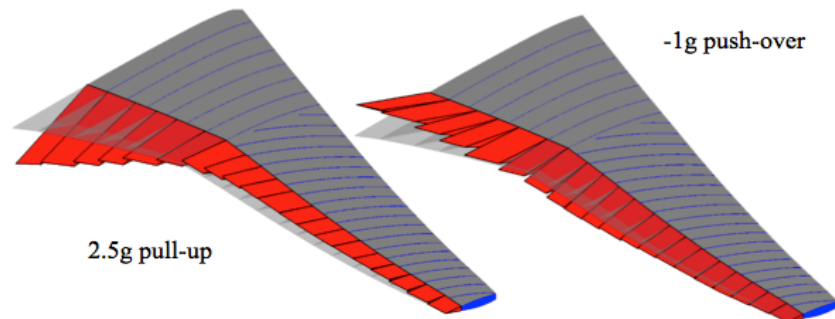

Figure 5. Optimal quasi-steady DMCS deflection scheduling across different load cases.

III. Testing of a Truss-Braced Wing in the TDT

The configuration studied in this aeroelastic test program is the Subsonic Ultra Green Aircraft Research (SUGAR) truss-braced wing (TBW), the result of a study by the Boeing Company [18] and shown in the left of Figure 6. The study included the development of a detailed full-scale finite element model (FEM) of the wing and center body. This model was used to optimize the wing subject to multiple design constraints including flutter. To validate the flutter predictions, an aeroelastically scaled wind tunnel model was designed, fabricated, and tested. Other goals of the wind tunnel test were to demonstrate flutter suppression and assess the control law effects on gust loads. The full-scale and model-scale FEMs along with the wind tunnel model design are described in detail in Refs. [19] and [20].

The TBW wind tunnel model was tested in the NASA Langley Transonic Dynamics Tunnel (TDT) from December 2013 to April 2014. Both open-loop and closed-loop data were acquired as part of this effort. The TBW wind tunnel test results showed that the flutter mechanism was primarily a coalescence of the 2nd bending mode and the 1st torsion mode near 10 Hz, as predicted by analysis. Results also showed a change in the flutter and limit cycle oscillation (LCO) boundary as angle of attack (AoA) was varied. Control laws designed using ASE models (derived

from experimental data and FEM models) were successful in suppressing flutter. A summary of the wind tunnel test and associated results is presented here.


Figure 6. SUGAR TBW vehicle concept (left) and illustration of the Transonic Dynamics Tunnel (right).

A. Transonic Dynamics Tunnel

The NASA Langley Transonic Dynamics Tunnel, depicted in the right of Figure 6, is a unique national facility dedicated to help identify, understand, and solve relevant aeroelastic and aeroservoelastic problems. The TDT is a closed-circuit, continuous-flow, variable-pressure, wind tunnel with a 16-foot square test section with cropped corners [3]. The tunnel uses either air or a heavy gas as the test medium and can operate at total pressures from near vacuum to atmospheric. It has a Mach number range from near zero to 1.2 and is capable of maximum Reynolds numbers of about 3 million per foot in air and 10 million per foot in heavy gas. The TDT is specially configured for flutter testing, with excellent model visibility from the control room and a rapid tunnel shutdown capability for model safety. Testing in heavy gas has important features over testing in air, such as improved model to full-scale similitude, higher Reynolds numbers, and reduced tunnel power requirements.

B. TBW Wind Tunnel Model

The TBW wind tunnel model was a fifteen-percent length scale, semi-span, sidewall mounted model based on the design described in Ref. [20]. The model consisted of several major components including the wing, strut, jury (vertical strut), flow-through nacelle, pylon, inboard and outboard ailerons, and fuselage. A photo of the model in the TDT is shown in Figure 7. The model wing span to the vehicle center line was 12.75 ft with an additional 2.25 inches added to the half fuselage (for the offset or peniche). The model was supported by a turntable and the model AoA could be varied between -3° and 5°. The wing, strut, and jury were aeroelastically scaled for testing in heavy gas, which resulted in a heavier, easier to build model with lower elastic mode frequencies, thereby minimizing actuator bandwith requirements. The components used a spar-pod design where the scaled stiffnesses was designed into the flanged aluminum spars, and the aerodynamic shape was provided by discrete fairings, or pods, mounted to the spars.
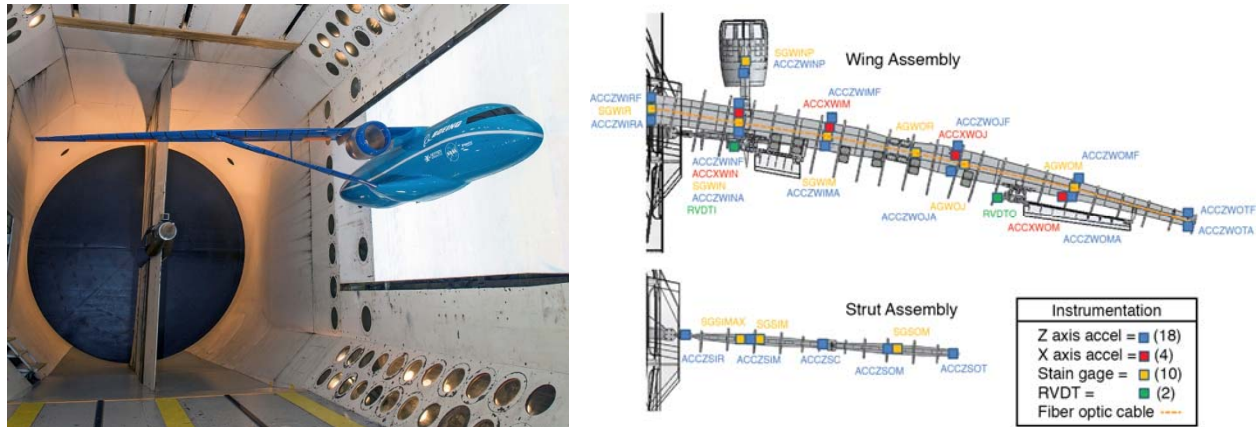
Figure 7. TBW wind tunnel model in the TDT (left) and model instrumentation (right).

Lead weights were attached to the wing spar in several locations so the wing had properly-scaled mass and moment of inertia. The aerodynamic fairings (pods) were made of graphite epoxy and attached to the spars using brackets. The nacelle and pylon were not structurally scaled, but had the correct mass and moment of inertia. The fuselage consisted of an aluminum internal structure with fiberglass skin panels. The wing had an inboard and an outboard high-bandwith aileron for use during the ASE portions of the wind tunnel test. The primary instruments for measuring aeroelastic response were 22 accelerometers and 10 strain gages as shown in Figure 7.

C. Wind Tunnel Testing

Testing of the TBW wind tunnel model took place intermittently over the span of several months and within this testing timeframe, a holiday break temporarily paused the testing. Upon resuming, a fouling problem was identified and fixed. This model change resulted in an inadvertent configuration change and the two configurations are herein referred to as pre-holiday and post-holiday. With the exception of several air checkout runs, all TBW data were acquired in heavy gas; only data acquired in heavy gas are presented here.

For open-loop flutter testing, the goal was to establish the Mach and dynamic pressure of flutter onset. Typical flutter testing in the TDT relies on naturally occurring tunnel turbulence to excite the model. Mach number and dynamic pressure are gradually increased along a total pressure (H) line until a flutter/LCO point is obtained. The determination of flutter is made visually by the test engineers, from strip chart observations, or from other stability assessments. Once a flutter point is obtained, the flow speed is reduced to stabilize the model. Repeating this process over multiple H-lines allows the test engineers to define the flutter/LCO onset boundary.

For each AoA tested, open-loop stable points were plotted on the TDT heavy gas operating envelope. Tunnel conditions where stable points were not obtained represent unstable regions, and approximate flutter boundaries are drawn on the plots. Flutter suppression control laws were used to pass through the unstable region and get to stable tunnel conditions, at higher Mach numbers, in order to define the back side of the onset boundary.

Example results of post-holiday flutter data for -3° AoA are shown in Figure 8. The acquired stable data points indicate a small unstable region approximately between M=0.73 and M=0.78 and dynamic pressures between 70 and 90 psf. The stable points above the unstable region indicate that the flutter mechanism is likely a hump mode as it re-stabilizes at higher dynamic pressures. Figure 9 shows the same flutter onset boundary and identifies points where the bypass valves were used or LCO was observed. Results for all other AoA can be found in Ref. [21].
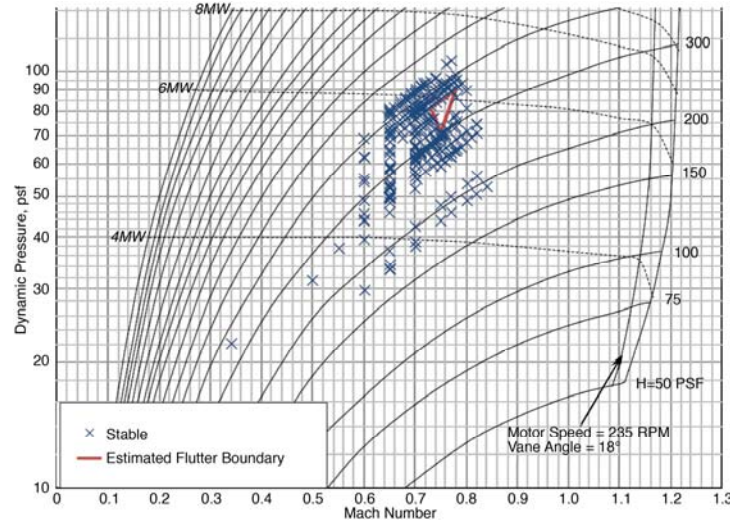
**Figure 8. TDT heavy gas boundary with stable points and post-holiday flutter boundary (AoA -3°).**

Comparison of pre-holiday and post-holiday flutter results is merited due to the inadvertent configuration change previously mentioned. Figure 10 shows pre- and post-holiday flutter onset boundaries for each of the four AoAs. Both sets of data show the nonlinear effect of AoA/loading on flutter onset. One of the key objectives of the SUGAR study was to refine the TBW configuration and reduce the uncertainty in the potential benefits, with specific focus on reducing the uncertainty of the wing weight. As a result of the findings from the open-loop wind tunnel test, the full-scale TBW design was updated, resulting in a small increase in wing weight, and therefore the TBW design is still a viable N+3 configuration.
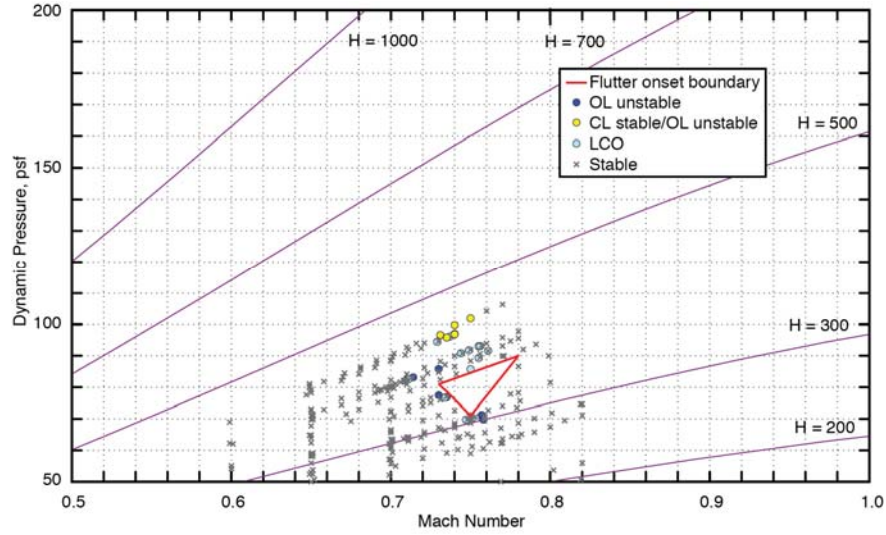
Figure 9. Close-up of post-holiday boundary with LCO and flutter points (AoA = -3°).

The primary objective of the closed-loop portion of the test was to demonstrate flutter suppression. Two sets of gain-scheduled control laws were developed; system ID based and FEM based. While performing closed-loop testing, periodically the loop was opened to assess open-loop stability. Example closed-loop results for -3° AoA are presented in Figure 11. At this AoA, it is clear that the controller was successful in stabilizing the model through the heart of the flutter onset boundary.
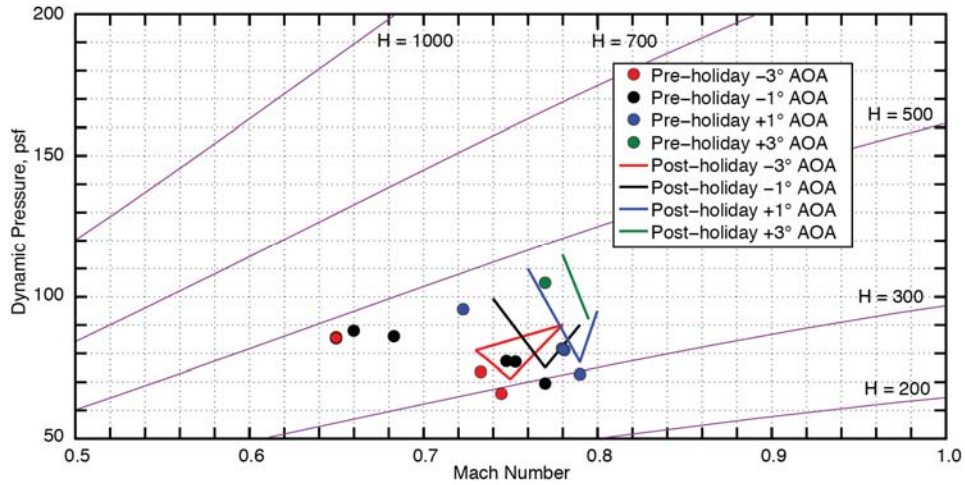
**Figure 10. Pre- and post- holiday combined flutter boundaries.**

IV. Numerical Modeling of a Truss-Braced Wing

This section presents a numerical companion study to the TBW wind tunnel testing of the previous section. Several aspects of the TBW configuration are non-traditional, and these features have a large impact on the types of aeroelastic analyses that are required. Such features include an increased aspect ratio (for drag reduction), increased wing span, thinner wing sections, and a reduction in wing sweep. While a thinner wing may result in greater flexibility, this effect is mitigated to some extent by the superior load bearing potential of the under-wing strut. The multiple load paths of a strut and jury reduce the bending moment supported by the inner wing and allow an inboard wingbox to be lighter, thinner and thus, more flexible. It also results in wing, strut, and jury members that are in tension or compression, rather than bending only.

9
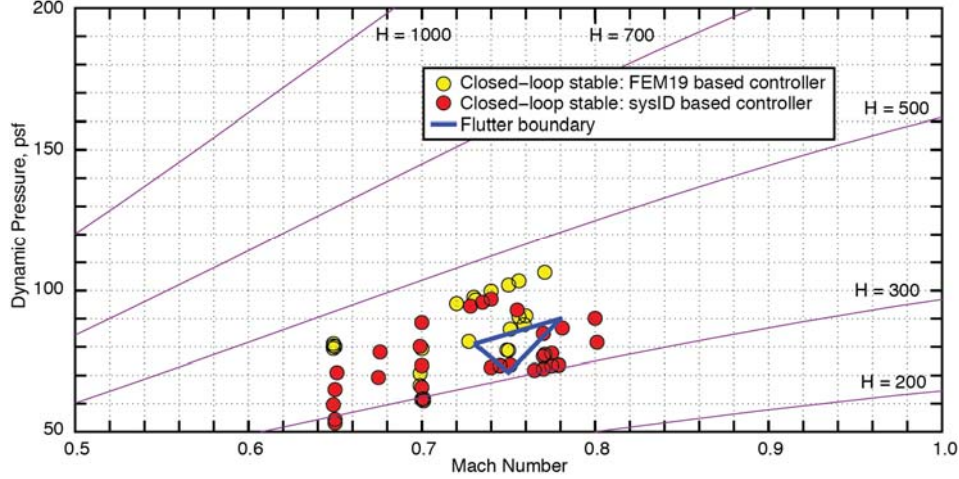
Figure 11. Flutter and closed-loop stable points (AoA = -3°).

The proximity of a wing, strut, jury, and engine nacelle flown at transonic speeds suggests the need for nonlinear higher fidelity tools to simulate the aerodynamic interaction. This aerodynamic interaction of components may also influence aeroelastic interactions. High-fidelity unsteady computational fluid dynamics has been recently used [22][23] to simulate the aeroelastic behavior of the Boeing SUGAR truss-braced wing wind tunnel model in Figure 7. In those references, time-accurate high-fidelity CFD is coupled with uncoupled structural eigenmodes. Beams are employed to model the wing, truss, jury, engine strut and trailing-edge control surfaces. The structural eigenmodes from that model are a linearization about non-linear pre-stressed static solutions. Aeroelastic solutions were also obtained at AoAs of -1° and 1° at transonic Mach numbers using the non-linear structural model and doublet lattice aerodynamics [23], via steady CFD corrections. The high-fidelity time-accurate simulations are performed with the Navier-Stokes code FUN3D [24] with a semi-infinite tetrahedral volume grid having 4.5 million nodes. The wind tunnel wall is treated as a symmetry plane, the surface mesh on which is seen in Figure 12.
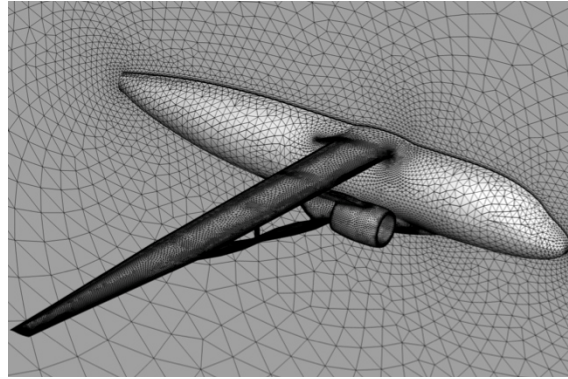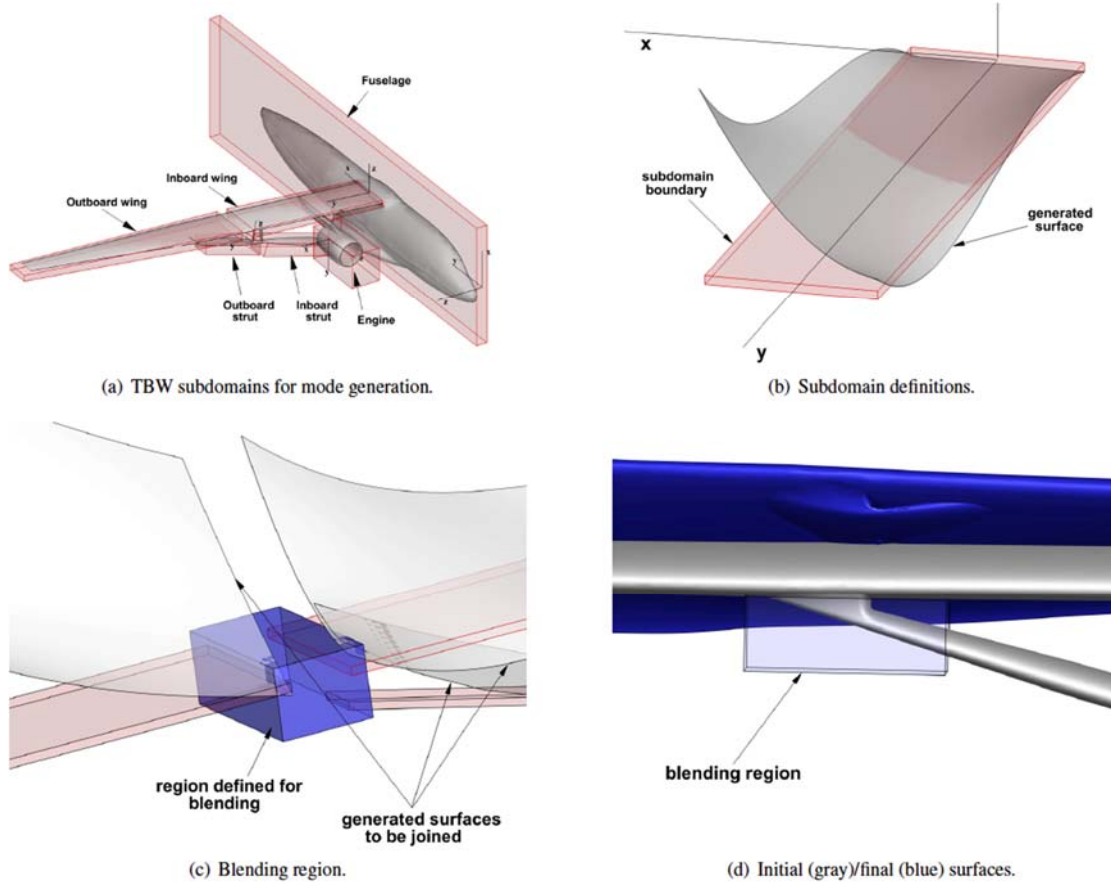

Figure 12. TBW CFD surface mesh.

For a vehicle with truss, jury, and wing connections, deflection and force transfer between a beam model and a high Reynolds number CFD mesh (dissimilar structural and fluid meshes) is a challenge. Both the linear flutter and the CFD aeroelastic simulations use a modal representation of the structure. In light of the structural model described earlier, the transfer of modal deflections is between a complex interconnection of multiply oriented beams and the aerodynamic surface nodes.   The method to transfer node deflections from the beam model to the CFD surface mesh is a simplification of that discussed in Ref. [22]. For this work, several intermediate steps and an intermediate coarse mesh have been eliminated.

The transfer of deflections from the beam nodes to the CFD surface mesh starts with regions in which a continuous mathematical approximation of the nodal deflections is defined. Six subdomain regions are defined, as shown in Figure 13a. Up to sixth order polynomial functions can be defined in local optimally oriented coordinate

systems, as shown in Figure 13b. The modal deflection, calculated in the local coordinate system, is transformed back into the global coordinate system. The polynomial approximation of the FEM nodal deflections is transferred to the final CFD mesh. Finally, a merge/blend step is performed between the subdomains (see Figure 13c), which smoothly joins subdomains into a continuously deflected surface. Additional details regarding the smoothing process used for blending are found in Ref. [22]. An example of the final product is shown in Figure 13d.


(a) TBW subdomains for mode generation.

(b) Subdomain definitions.

(c) Blending region.

(d) Initial (gray)/final (blue) surfaces.

Figure 13. Beam model deflection transfer to CFD surface.

A. Flutter Boundaries

For the linear flutter analysis, NASTRAN's non-iterative p-k method is used, as described in Ref. [25]. A matched set of densities and velocities are calculated based on the heavy gas test medium. Steady aerodynamic corrections based on CFD results are utilized to improve the fidelity of the aerodynamics used in the simulations. Figure 14 presents flutter onset results at 0° AoA for two versions of the FEM model, termed here v.19 and v.20 (where v.19 is for the pre-holiday configuration referenced above, and v.20 accounts for changes due to fouling). The unloaded vibration modes and frequencies are used for these flutter analyses. Note that experimental LCO conditions at -1° and 1° AoA are shown in the figure for reference, as well as linear (p-k) flutter results and flutter boundaries estimated from the CFD runs.

Ref. [22] presents solutions for unloaded conditions at 0° AoA, using the v.19 FEM modes. The same approach is used here for conditions at 0° AoA using the v.20 FEM. To make a consistent comparison with these high-fidelity simulations, p-k flutter calculations are also performed using unloaded v.19 modes. A comparison of the flutter onset boundaries using the v.19 and v.20 FEMs can be seen in Figure 14. The model changes made in going from v.19 to v.20 have a significant effect on flutter onset. The fundamental flutter mechanism does not change, still being a coalescence of modes 3 (2nd bending) and 4 (1st torsion) at a frequency near 10 Hz [22]. However, the dynamic pressure at which flutter onset occurs is significantly higher using the v.20 as opposed to the v.19 FEM. The increase in flutter onset dynamic pressure can be accounted for by the larger difference in the 3rd and 4th mode frequencies in v.20, requiring a higher dynamic pressure at which the two modes coalesce.

As for the time-accurate high-fidelity aeroelastic simulations, there is a significant difference in LCO onset between the v.19 and v.20 FEMs. Besides the general increase in the dynamic pressure at LCO onset using the v.20 FEM, there is a more profound difference in the LCO onset boundaries above Mach 0.80. With v.20, no sustained LCO was found at Mach 0.82 until a dynamic pressure of 110 psf. The estimated LCO onset line for v.20 and the conditions with LCO and without LCO (closed/open delta symbol) in Figure 14 are at 0° AoA. Although not shown, the lack of sustained LCO at Mach 0.82 below 100-110 psf was also seen in v.20 simulations at -1° and 1° AoA. Thus, a sharp rise in flutter/LCO onset at all AoAs occurs between Mach 0.78 and 0.82. This is a very different behavior than was computed with FEM v.19.
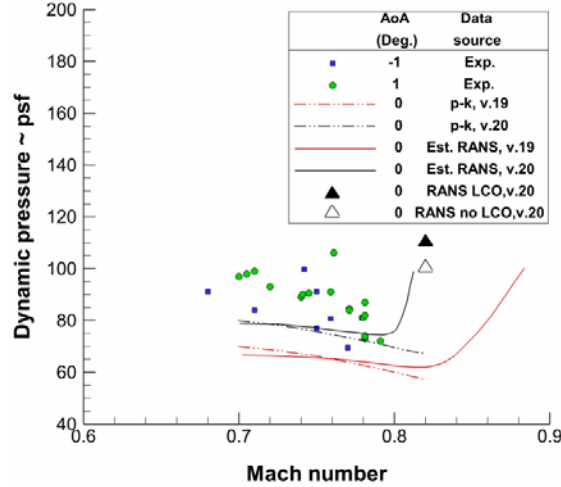
Figure 14. Linear, nonlinear, and experimental flutter onset boundaries.

The time-accurate CFD RANS (Reynolds averaged Navier-Stokes) analysis in Ref. [22], using the v.19 FEM, found LCO onset at fairly low dynamic pressures beyond Mach 0.82 (see the solid red line in Figure 14). The LCO onset using v.20 is much more consistent with the flutter onset presented by Coggin et al. [26], also confirming that the flutter/LCO onset is very sensitive to the mass and/or stiffness distribution of the structure.

The CFD and p-k flutter instability boundaries shown in Figure 15, at -1° and 1° AoA, also show a sensitivity to AoA. This can largely be accounted for by the fact that the positive wing loading at 1° results in higher frequencies in the first two out-of-plane bending modes, in particular mode 3. Negative wing loading increases the frequency of the out-of-plane bending modes, but not to the extent that positive loading does, thus accounting for the difference in flutter onset dynamic pressure at -1° and 1° AoA. It also accounts for the fact that the flutter onset boundaries at -1° and 1° AoA are at higher dynamic pressures than that for 0° AoA.
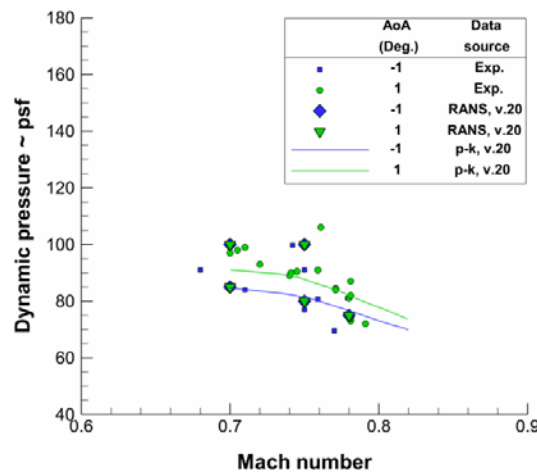
Figure 15. Linear, nonlinear, and experimental flutter onset boundaries at -1° and 1° AoA.

B. LCO Amplitudes

Time-accurate high-fidelity RANS simulations at -1°, 0°, and 1° AoA were performed at transonic conditions and several dynamic pressures, as shown in Figure 16. Three conditions are near flutter onset (Mach 0.70, 0.75 and 0.78) while two conditions are at much higher dynamic pressures (100 psf at Mach 0.70 and 0.75). Limit cycle oscillation (as indicated by wingtip acceleration amplitudes) rather than outright instability are indicated by the RANS computations. The RANS LCO amplitudes at AoAs of -1° and 1° are smaller than at 0° in most cases. The larger amplitude at 0° AoA is consistent with the linear p-k results, in that flutter onset at 0° is at a lower dynamic pressure than the flutter onset at AoAs of -1° and 1°. Note also that the LCO amplitude is larger at AoA of -1° than at 1°. This is also consistent with the present linear flutter solutions, and those of Coggin et al. [26], which show flutter onset at -1° at a lower dynamic pressure than at 1°.

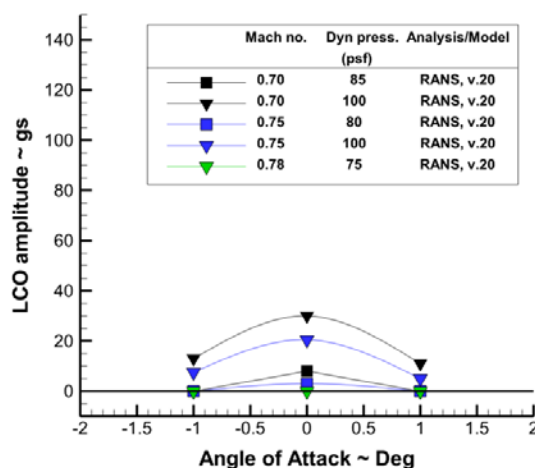|	Mach no.	Dyn press. (psf)	Analysis/Model
■	0.70	85	RANS, v.20
▼	0.70	100	RANS, v.20
■	0.75	80	RANS, v.20
▼	0.75	100	RANS, v.20
▼	0.78	75	RANS, v.20

Figure 16. TBW limit cycle oscillations at various flight conditions.

V. Numerical Modeling of a Low-Boom Supersonic Configuration

The configuration under study in this research effort is shown in Figure 17 (artist rendering). This configuration, along with a detailed finite element model, was developed by Lockheed Martin, and will be referred to as the N+2 configuration (two generations from present state). The configuration has three engines: one mounted aft and on top while the other two are mounted below and close to the fuselage. This arrangement precludes aeroelastic issues related to wing-mounted engines, but large masses attached to the tail of a flexible fuselage may pose additional problems. The vehicle cruises at a Mach of 1.7, and has a range above 5000 nm. The highly detailed structural model of the vehicle (described in Ref. [27], and consisting of skins, ribs, spars, bulkheads, and longerons) was sized by Lockheed Martin across a variety of maneuver, gust, and landing load conditions. Stress, buckling, and manufacturing constraints are all enforced during the optimization process, and the final structure is composed of 55% composites, 26% aluminum, 16% titanium, and 3% steel.

**Figure 17. Artist's concept of the Lockheed-Martin N+2 configuration.**

Linear flutter results (doublet lattice method for subsonic flow, and the oscillatory lifting surface theory ZONA51 for supersonic), for a range of conditions including with/without fuel and symmetric/anti-symmetric mode shapes, indicate [27] that flutter does not occur within the flight envelope (including a 15% speed margin) for this configuration. However, linear techniques have been known to be non-conservative in the transonic range (the

limits of this range are not clear for this non-traditional configuration), necessitating the use of higher-fidelity CFD-based tools.

C. Steady CFD Results

Results are provided in this section using the inviscid FUN3D solver [24], for a series of unstructured grids with varying mesh density. Within the code, the unsteady Navier-Stokes equations are discretized over the median dual volume surrounding each mesh point, balancing the time rate of change of the averaged conserved variables in each dual volume with the flux of mass, momentum and energy through the instantaneous surface of the control volume. Coarse (5.4 million) and fine (57.5 million) grid results are presented in Figure 18 for a rigid vehicle in cruise. A quantitative comparison of these solutions (along with a medium grid) at a near-field location 8.25 half-spans beneath the vehicle indicate an acceptable level of convergence between the medium and fine grids.
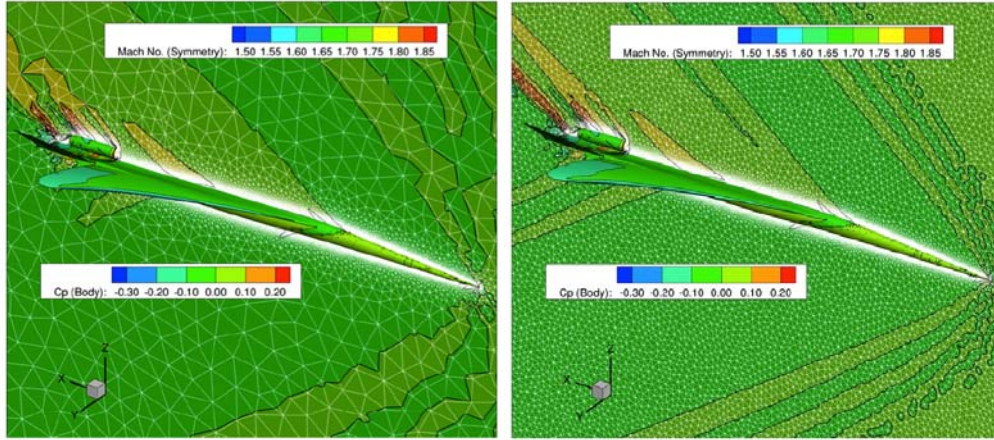
Figure 18. Coarse grid (left) and fine grid (right) steady Euler FUN3D analysis of a rigid vehicle during cruise.

Static aeroelastic results from the coarse grid (not the same coarse grid utilized in Figure 18, as this grid was modified and adapted in order to perform accurate sonic boom analyses) are shown in Figure 19, in terms of pressures along the near-field slice beneath the wing. This is done using the first 25 flexible vibration modes. Six inches of static deflection at the wing tip and tail are noted (though not shown in the figure), which tends to unload the wing. A modified pressure distribution is noted along the wing, as well as along the near-field slice shown in Figure 19. This result suggests a strong relationship between static aeroelastic deformation and the sonic boom signature, as the two results are run at the same flow condition (AoA, dynamic pressure) otherwise.
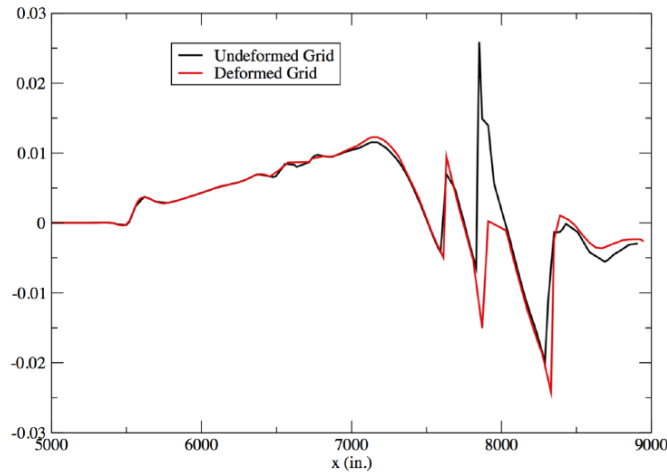
Figure 19. Near-field pressure distribution for the deformed and un-deformed configurations.

14

D. Reduced Order Modeling

The development of reduced order models (ROMs) is also underway for the N+2 configuration, which may provide high-fidelity (CFD-based) aeroelastic results at a small fraction of the computational cost. Recent advances in parallel processing techniques, algorithms, and computer hardware have provided substantial reductions in the cost of a vehicle-level aeroelastic analysis, but utilizing CFD-based tools in a formal design environment (parametric variations, numerical optimization) is still prohibitive. ROMs may enable these studies; the reduced computational cost (and turn-around time) should also improve our understanding of the complex aeroelastic and aeroservoelastic physics inherent in non-traditional aircraft such as the N+2 configuration in Figure 17.

Numerical details of the ROMs utilized here are described in Refs. [28] and [29]. Though not shown here, dynamic aeroelastic results (time histories of modal amplitudes) match well for all modes, for a given Mach number and dynamic pressure. A major benefit of this ROM technology is the ability to rapidly generate an aeroelastic root locus plot that reveals the aeroelastic mechanisms occurring at that flight condition. A root locus plot is a common tool for linear aeroelasticity, but typically unavailable for higher fidelity CFD-based aeroelastic results. These plots can provide substantial insights into the aeroelastic mechanisms that may result in unstable flutter behavior.

The computational cost of generating a ROM solution consists of one full FUN3D solution that is used to generate the ROM at that Mach number. For this case, the full FUN3D solution runs for three hours and consists of 2400 time steps. Once this solution is available, a ROM can be generated and then used to generate all the aeroelastic responses at all dynamic pressures. In comparison, a full FUN3D analysis at each dynamic pressure requires two full FUN3D solutions: a static aeroelastic response (10 hours) and a dynamic aeroelastic response (18 hours). Therefore, full FUN3D solutions for 20 dynamic pressures would require 560 hours of computer time. By contrast, a ROM-based root locus plot across 20 dynamic pressures is generated in seconds.

## VI.   The Aeroelastic Prediction Workshop

The aeroelastic prediction workshop series is intended to provide an open forum, to encourage transparent discussion of results and processes, to promote best practices and collaborations, and to develop analysis guidelines and lessons learned. The willingness of analysis teams to be open about all aspects of their computations is the underpinning for a more rapid advancement in the state of the art or state of the practice, especially since no comprehensive aeroelastic benchmarking validation standard currently exists, greatly hindering validation objectives.

The fundamental technical challenge of computational aeroelasticity (CAE) is to accurately predict the coupled behavior of the unsteady aerodynamic loads and the flexible structure. Numerous organizations have developed analytical methods and codes to address this issue, each conducting their own validation effort. Twenty-four analysis teams from 10 nations compared results from their own CAE codes in the first AIAA Aeroelastic Prediction Workshop (AePW-1), held April 21-22, 2012, [30][31][32]. AePW-1 served as a step in assessing the state-of-the-art of computational methods for predicting unsteady flow fields and aeroelastic response. AePW-2 builds on those experiences, and will be held in conjunction with the SciTech 2016 conference in San Diego, California. The objective in presenting this information is to solicit worldwide participation in assessment of the state of the art in aeroelastic computational methods.

Members of the organizing committee have examined the results from AePW-1, and performed subsequent data reduction and analyses to select test cases that are hopefully of interest to aeroelasticians and computational aerodynamicists from different organizations. Interested parties should visit the workshop website (https://nescacademy.nasa.gov/workshops/AePW2/public/) and consult SciTech 2015 reference [33] for additional information. The workshop will include open forums designed to encourage transparent discussion of results and processes, promote best practices and collaborations, and develop analysis guidelines and lessons learned.

## A. Workshop Overview and Formulation

AePW-1 concentrated on the analysis of the unsteady flow phenomena with weak coupling between aerodynamics and the structure. AePW-2 extends the benchmarking effort to aeroelastic flutter solutions (i.e., strong coupling between aerodynamics and the structure). The configuration chosen for the next workshop is the Benchmark Supercritical Wing (BSCW) shown in Figure 20. The primary analysis condition has been chosen such that the influence of separated flow is considered to be minimal, yet a shock is still present. This is a step backwards in flow complexity from the BSCW cases analyzed in AePW-1. The goal in moving to the lower transonic Mach number is to have analysis teams progress through unforced system analyses, forced oscillation solutions and flutter analyses. Revisiting the AePW-1 analysis condition is included in AePW-2 as an optional case, also extending it to include flutter solutions.
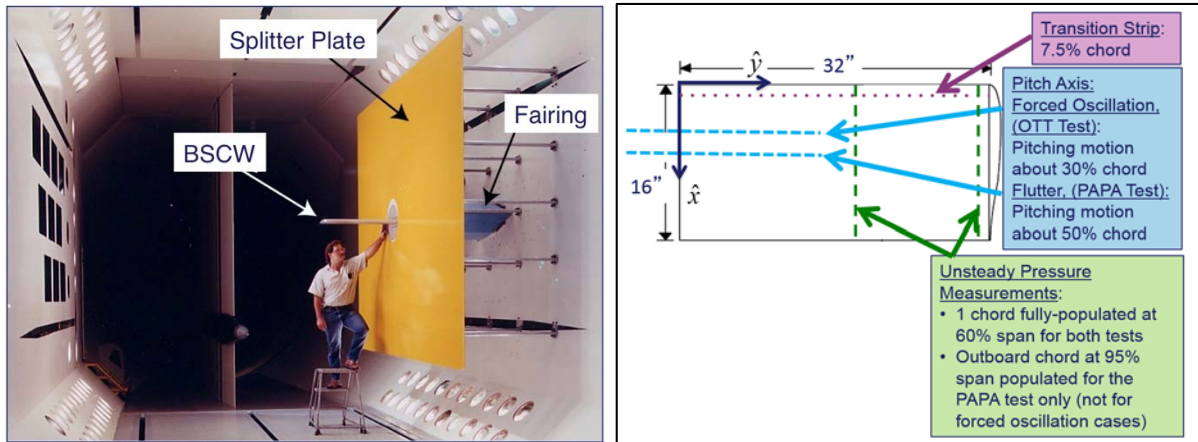
Figure 20. BSCW model.

From AePW-1 there were several lessons learned that have guided the formulation of AePW-2. One lesson learned was that there were too many analysis configurations, diluting the effort rather than distilling the information. Only one configuration, BSCW, will be analyzed for AePW-2. Another lesson learned was that a simple benchmarking test case must be part of the analysis matrix. For AePW-2, low transonic Mach numbers will be the focus. The remainder of this section discusses technical observations relevant to the BSCW configuration and offers the experiences of the organizing committee members to workshop participants.

The BSCW case from the first workshop was Mach 0.85 at 5° angle of attack. There was significant scatter in even the steady results reported by the different analysis teams. The computational results showed some differences from the experimental data as depicted in Figure 21. While the analyses each predicted an upper surface shock, the location of that shock varied by approximately 20% of the chord, with all solutions except one predicting the shock further aft than indicated by experimental data. In the region aft of the upper surface shock, the computational results for the pressure distribution were fairly grouped, however, they disagreed with the experimental data in terms of the shape of the distribution and pressure level. The lower surface shock predictions were more consistent, with approximately 5% chord-wise variation. In the aft cusp region of the airfoil, the computational results all had roughly the same distribution shape, but again disagreed with the experimental data both in shape and value.
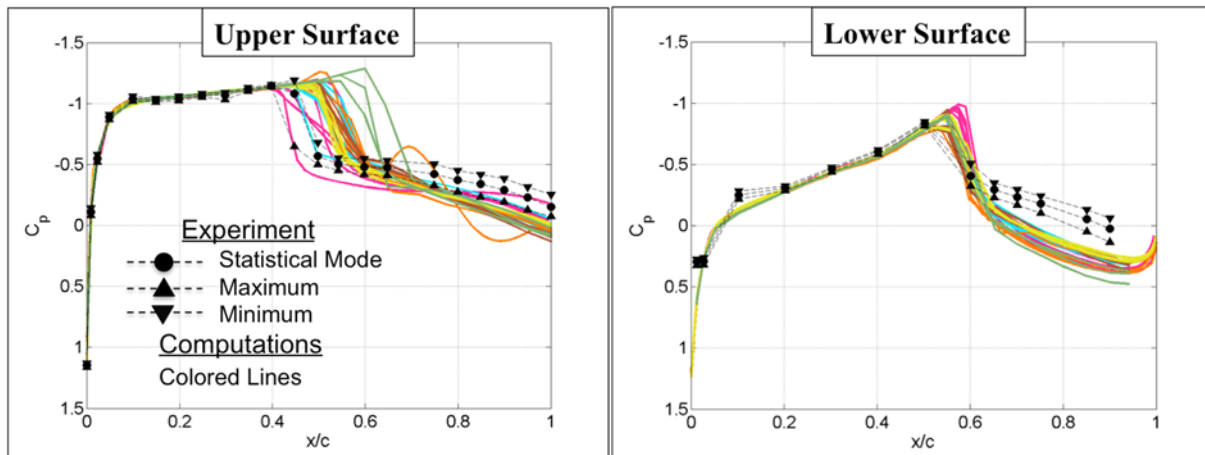
Figure 21. AePW-1 BSCW collective computational results at 60% wing span, Mach 0.85, α = 5°.

During the first workshop, the solution procedure for obtaining the unforced system responses for this separated flow case were discussed. The majority of the unforced system solutions presented were not performed in a time accurate manner, i.e., they were performed as steady calculations. There was considerable discussion around the idea that there was likely a significant enough region of separated flow to make this problem inherently unsteady,

16

even for the unforced, previously called "steady", system. At the time of the workshop, no assessment of the extent of flow separation on this configuration had been performed.

Subsequent to the first workshop, two things were done to examine this. First, the experimental data was examined; data corresponding to the AePW-1 analysis condition indicated that there was separation behind the upper surface shock that extends to the trailing-edge, and on the lower surface, the separation originates in the cusp region and extends to the trailing-edge [31]. Second, time-accurate unsteady RANS analyses were performed on the unforced wing. These preliminary results, which have not been previously reported, show that the prediction of the upper surface shock location does not stabilize to a single position, but rather varies over a range. These new results will be reported at AePW-2, and are mentioned here for those analysis teams investigating the optional case.

There was also considerable discussion at the workshop regarding assessing temporal convergence. Numerous participants expressed the view that more information on temporal convergence of both the unforced and the forced oscillation solutions needed to be shown in order to assess the goodness of the results. Subsequent analyses have shown great sensitivity to temporal convergence and sub-iteration specification, including changing the system from stable (flutter-free) to unstable (flutter). These analysis results will be reported at AePW-2; they are mentioned here to provide further motivation for teams to focus their early efforts in flutter analysis on the influence of temporal convergence.

A third important discussion at AePW-1 centered around the shortcomings of the methods being applied. While the previous two concerns could be called shortcomings of the application of the methods, it was also discussed that RANS solutions cannot capture separated flow effects. It was suggested that higher fidelity methods should be applied at this test condition. Subsequent work has been performed using EDGE, an unstructured CFD solver, in a hybrid RANS-LES (large eddy simulation) mode [34]. Work is on-going with several higher fidelity codes and will be reported as part of the next workshop.

B. BSCW Configuration Details

The Benchmark Supercritical Wing (BSCW) model, shown in Figure 20, was tested in the NASA Langley Transonic Dynamics Tunnel in two test entries. The most recent test served as the basis for AePW-1; testing was performed on the oscillating turntable (OTT) [35], which provided forced pitch oscillation data. A prior test was performed on a flexible mount system, denoted the pitch and plunge apparatus (PAPA). In each test, the model was mounted to the same large splitter plate, sufficiently offset from the wind tunnel wall (40 inches) to be outside of any tunnel wall boundary layer [36]. Aeroelastic testing was performed for the model on the PAPA, where the mount system provides low-frequency flexible modes that emulate a plunge mode and a pitch mode. The BSCW/PAPA data consists of unsteady data at flutter points and steady data on a rigidified apparatus at the flutter conditions. Data from both tests will be utilized for comparison with simulation data in AePW-2.

The model's instrumentation includes chord-wise rows of in-situ unsteady pressure transducers; for the BSCW/PAPA test, there were rows at the 60% and 95% span stations. For the BSCW/OTT test, only the 60% span station test row was populated with transducers.

C. Planned AePW-2 Workshop Simulations

Workshop simulations will include three types of results, involving three types of computations. Steady results will be generated at a fixed Mach number and angle of attack combination. The steady results will be compared using pressure coefficients and integrated loads. Forced pitching oscillation results will be generated at a set of specified frequencies. Frequency response functions (FRFs) of pressure due to displacement/rotation will be used as the comparison quantities. The workshop simulations will include aeroelastic computations to identify the flutter condition, pressure distributions and frequency response functions both sub-critically and at flutter. The planned simulation cases are described in Table 1. For each of the cases, only the dynamic results type is listed in the Table 1. For each simulation, the steady solution results for the rigid structure are also desired. Since the flutter test case was not part of the AePW-1 workshop, the paragraph below describes the requirements for reporting of the computational flutter results.

It is anticipated that the following quantities will be provided by analysis teams for comparison among the computational results and with experimental data.
- Frequency response function of pressure coefficients due to pitch angle at 60% and 95%, as functions of non-dimensional chord location
- Displacement time histories of the wing leading- and trailing-edges at 32 inch wing span
- Pitch rotation angle time history: Note, because the wing itself is rigid, the results at all span stations should be nearly identical. However, for consistency among analysis teams, please extract the results at 95% span.
- Pressure coefficients versus time and chord location, at 60% span upper & lower surfaces

- Pressure coefficients versus time and chord location, at 95% span upper & lower surfaces
- Vertical cuts through the pressure field (i.e., cutting planes) at 60% and 95% span, taken over 1 cycle of oscillation at the flutter dynamic pressure only, that is, only for the neutrally stable case. It is requested that the cuts be made at the rate of approximately 12 cuts per cycle.
- Total wing lift and pitching moment coefficients; time histories rather than mean values are requested.
- Sectional lift and pitching moment coefficients at 60% span; time histories rather than mean values are requested.
- Sectional lift and pitching moment coefficients at 95% span; time histories rather than mean values are requested.

Table 1. AePW-2 Workshop Cases.

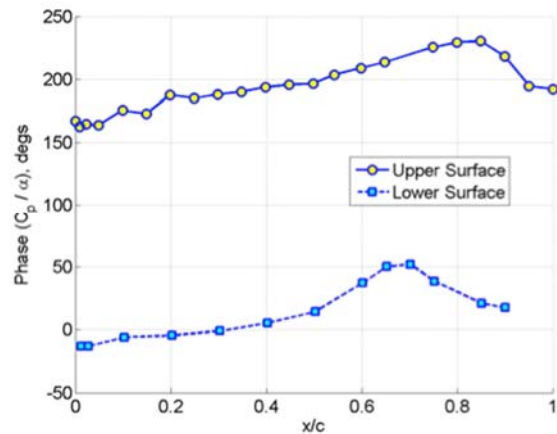|	Case 1	Case 2	Optional Case 3A	Optional Case 3B	Optional Case 3C
Mach	0.7	0.74	0.85	0.85	0.85
AoA	3°	0°	5°	5°	5°
Dynamic Results Type	Forced Oscillation f = 10 Hz, $|\theta|$=1°	Flutter	Unforced Unsteady	Forced Oscillation f = 10 Hz, $|\theta|$=1°	Flutter
Notes	- Attached flow -OTT exp. data -R-134a	-Flow state (?) -PAPA exp. data -R-12	-Separated flow -OTT exp. data -R-134a	-Separated flow -OTT exp. data -R-134a	-Separated flow -No exp. data -R-134a

D. Experimental Data

The experimental data sets being provided for comparison with the simulation results are derived from the two separate wind tunnel test campaigns. Unforced system simulation results will be compared with experimental data using the statistical data available from the BSCW/PAPA test, and information calculated from time history data for the BSCW/OTT test.

The frequency response functions (FRFs) between the pressure coefficients and the pitch angle have been computed from the experimental data at the forced oscillation frequency. The magnitude and phase are shown for the forced oscillation data sets in Figure 22. Experimentally determined flutter points are available for comparison with the results of simulation. Example plots shown in Figure 23, were produced using previously published data [37]. The figure shows the frequency response functions (between pressure and wing rotation) at the flutter condition. For the flutter simulations, flutter conditions and FRFs will be the direct comparisons between the computational and experimental results.
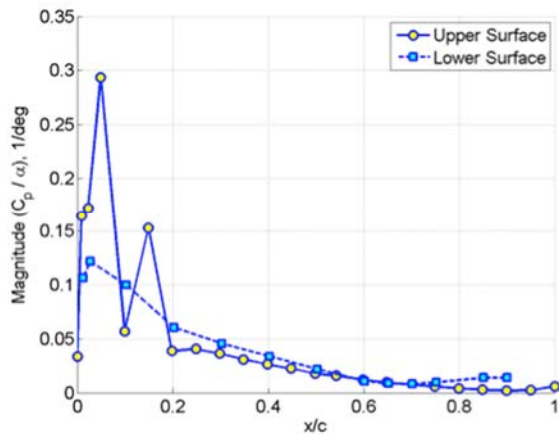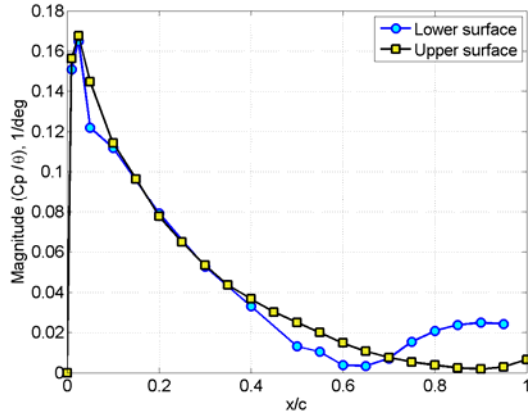

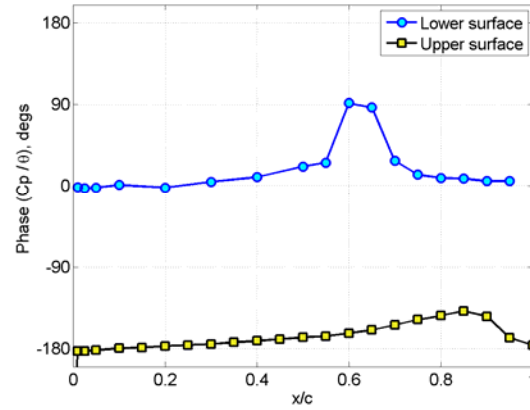(a) FRF Magnitude, Case #1: Mach 0.7, α = 3°, q = 170 psf   (b) FRF Phase, Case #1: Mach 0.7, α = 3°, q = 170 psf

Figure 22. Experimental data: Frequency response function of pressure coefficients due to angle of attack at 10Hz, 60% wing span, Case #1.

(a) Magnitude at 60% Span Station

(b) Phase at 60% Span Station

Figure 23. Experimental data: frequency response function magnitude and phase of surface pressure coefficient at flutter condition: q = 168.8 psf, Mach 0.74, α = 0°, Case #2.

VII.   Conclusions

This paper has provided an overview of recent and ongoing research activities pertaining to fixed wing aeroelasticity and aeroservoelasticity within the NASA Langley Aeroelasticty Branch. Several research efforts are summarized here for a wide range of aeroelastic configurations (and NASA projects), including computational analysis, experimental wind tunnel testing, design optimization, and validation/verification efforts.

Future civil air transport configurations, whether subsonic or supersonic vehicles, will be required to handle expected increases in air traffic in an economical and environmentally responsible manner. These factors are enabled by engineered reductions in fuel burn, structural weight, and (in the case of supersonic flight) sonic boom signature. It is expected that substantial improvements in these metrics will be obtained with highly-flexible non-traditional configurations, for which aeroelastic and aeroservoelastic physics are important design drivers. The Aeroelasticity Branch, in collaboration with academia, industry, and other government laboratories, is well-positioned to provide strong contributions to this effort, and help fully exploit and control aeroelasticity in the next generations of civil air transport.

Acknowledgements

References

[1]   Perry, B., Noll, T., "Activities in Aeroelasticity at NASA Langley Research Center," *ASME International Symposium on Fluid-Structure Interactions, Aeroelasticity, Flow-Induced Vibration, and Noise*, Dallas, TX, November 16-21, 1997.

[2]   Noll, T., Perry, B., Gilbert, M., "Recent Activities in Aeroservoelasticity at the NASA Langley Research Center," NASA TM 101582, 1989.

[3]   Cole, S., Garcia, J., "Past, Present, and Future Capabilities of the Transonic Dynamics Tunnel from an Aeroelasticity Perspective," *AIAA Dynamics Specialists Conference*, Atlanta, GA, April 5-6, 2000.

[4]   Cole, S., Noll, T., Perry, B., "Transonic Dynamics Tunnel Aeroelastic Testing in Support of Aircraft Development," *Journal of Aircraft*, Vol. 40, No. 5, pp. 820-831, 2003.

[5]   Cole, S., Keller, D., Piatak, D., "Contributions of the NASA Langley Transonic Dynamics Tunnel to Launch Vehicle and Spacecraft Development," *AIAA Dynamics Specialists Conference*, Atlanta, GA, April 5-6, 2000.

[6]   Kvaternik, R., "A Historical Overview of Tiltrotor Aeroelastic Research at Langley Research Center," NASA TM 107578, 1992.

[7]   Yeager, W., Kvaternik, R., "Contributions of the Langley Transonic Dynamics Tunnel to Rotorcraft Technology and Development," AIAA Paper 2000-1771, 2000.

[8]   Vassberg, J., DeHaan, M., Rivers, S., Wahls, R., "Development of a Common Research Model for Applied CFD Validation Studies," *AIAA Applied Aerodynamics Conference*, Honolulu, Hawaii, August 10-13, 2008.

[9]   Stanford, B., Wieseman, C., Jutte, C., "Aeroelastic Tailoring of Transport Wings Including Transonic Flutter Constraints," *AIAA SciTech Conference*, Kissimmee, FL, January 5-9, 2015.

[10] Taminger, K., Hafley, R., "Electron Beam Freeform Fabrication: A Rapid Metal Deposition Process." *Proceedings of the 3rd Annual Automotive Composites Conference*, Troy, MI, September 9-10, 2003.

[11] Niu, M., *Airframe Structural Design*, Conmilit Press Ltd., Hong Kong, 1988.

[12] Birman, V., Byrd, L., "Modeling and Analysis of Functionally Graded Materials and Structures," *Applied Mechanics Reviews*, Vol. 60, No. 5, pp. 195-216, 2007.

[13] Lukaszewicz, D., Ward, C., Potter, K., "The Engineering Aspects of Automated Prepreg Layup: History, Present and Future", *Composites: Part B*, Vol. 43, pp. 997-1009, 2012.

[14] Locatelli, D., Mulani, S., Kapania, R., "Wing-Box Weight Optimization Using Curvilinear Spars and Ribs (SpaRibs)," *Journal of Aircraft*, Vol. 48, No. 5, pp. 1671-1684, 2011.

[15] Stanford, B., Dunning, P., "Optimal Topology of Aircraft Rib and Spar Structures Under Aeroelastic Loads," *Journal of Aircraft*, to appear.

[16] Dunning, P., Stanford, B., Kim, H., "Level-Set Topology Optimization with Aeroelastic Constraints," *AIAA SciTech Conference*, Kissimmee, FL, January 5-9, 2015.

[17] Stanford, B., "Optimization of an Aeroservoelastic Wing with Distributed Multiple Control Surfaces," *AIAA Aviation Conference*, Dallas, TX, June 22-26, 2015, to appear.

[18] Bradley, M., Droney, C., "Subsonic Ultra Green Aircraft Research: Phase 1 Final Report," NASA CR-2011-216847, 2011.

[19] Allen, T., "SUGAR Truss Braced Wing Full Scale Aeroelastic Analysis and Dynamically Scaled Wind Tunnel Model Development," *AIAA SciTech Conference*, Kissimmee, FL, January 5-9, 2015.

[20] Bradley, M., Droney, C., Allen, T., "Subsonic Ultra Green Aircraft Research: Phase II Final Report," NASA CR NNL08AA16B, 2014.

[21] Scott, R., Allen, T., Funk, C., Castelluccio, M., Sexton, B., Claggett, S., Dykman, J., Coulson, D., Bartels, R., "Aeroservoelastic Wind-Tunnel Testing of the SUGAR Truss Braced Wing Wind-Tunnel Model," *AIAA SciTech Conference*, Kissimmee, FL, January 5-9, 2015.

[22] Bartels, R., Scott, R., Funk, C., Allen, T., Sexton, B., "Computed and Experimental Flutter/LCO Onset for the Boeing Truss-Braced Wing Wind-Tunnel Model," *AIAA Aviation Conference*, Atlanta, GA, June 16-20, 2014.

[23] Bartels, R., Scott, R., Allen, T., Sexton, B., 'Aeroelastic Analysis of SUGAR Truss-Braced Wing Wind-Tunnel Model Using FUN3D and a Nonlinear Structural Model," *AIAA SciTech Conference*, Kissimmee, FL, January 5-9, 2015.

[24] Biedron, R., Thomas, J., "Recent Enhancements to the FUN3D Flow Solver for Moving Mesh Applications," Orlando, FL, January 5-8, 2009.

[25] Rodden, W., Harder, R., Bellinger, E., "Aeroelastic Addition to NASTRAN," NASA CR 3094, 1979.

[26] Coggin, J., Kapania, R., Zhao, W., Schetz, J., Hodigere-Siddaramaiah, V., Allen, T., Sexton, B., "Nonlinear Aeroelastic Analysis of a Truss Braced Wing Aircraft," *AIAA SciTech Conference*, National Harbor, MD, January 5-9, 2014.

[27] Silva, W., De La Garza, A., Zink, P., Bounajem, G., Johnson, J., Buonanno, M., Sanetrik, M., Chwalowski, P., Florance, J., Yoo, S., Kopasakis, G., Hur, J., Christhilf, D., "An Overview of the NASA High Speed ASE project: Aeroelastic Analysis of a Low-Boom Supersonic Configuration," *AIAA SciTech Conference*, Kissimmee, FL, January 5-9, 2015.

[28] Silva, W., "Simultaneous Excitation of Multiple-Input/Multiple-Output CFD-Based Unsteady Aerodynamic Systems," *Journal of Aircraft*, Vol. 54, No. 4, pp. 1267-1274, 2008.

[29] Silva, W., Vatsa, V., Biedron, R., "Development of Unsteady Aerodynamic and Aeroelastic Reduced-Order Models Using the FUN3D Code," *International Forum on Aeroelasticity and Structural Dynamics*, Seattle, WA, June 21-25, 2009.

[30] Schuster, D., Chwalowski, P., Heeg, J., Wieseman, C., "Summary of Data and Findings from the First Aeroelastic Prediction Workshop," ICCFD7, July 2012.

[31] Heeg, J., Chwalowski, P., Schuster, D., Dalenbring, M., Jirasek, A., Taylor, P., Mavriplis, D., Boucke, A., Ballmann, J., Smith, M., "Overview and Lessons Learned from the Aeroelastic Prediction Workshop," *International Forum on Aeroelasticity and Structural Dynamics*, Seattle, WA, June 21-25, 2009.

[32] Heeg, J., Chwalowski, P., Schuster, D., Dalenbring, M., "Overview and Lessons Learned From the Aeroelastic Prediction Workshop," *AIAA Structures, Structural Dynamics, and Materials Conference*, Boston, MA, April 8-11, 2013.

[33] Heeg, J. Chwalowski, P., Schuster, D., Raveh, D., Jirasek, A., Dalenbring, M., "Plans and Example Results for the 2nd AIAA Aeroelastic Prediction Workshop," *AIAA SciTech Conference*, Kissimmee, FL, January 5-9, 2015.

[34] Dalenbring, M., Jirasek, A., Heeg, J., Chwalowski, P., "Initial Investigation of the BSCW Configuration using Hybrid RANS-LES modeling," *AIAA Structures, Structural Dynamics, and Materials Conference*, Boston, MA, April 8-11, 2013.

[35] Piatak, D., Cleckner, C, "Oscillating Turntable for the Measurement of Unsteady Aerodynamic Phenomena," *Journal of Aircraft*, Vol. 40, No. 1, pp. 345-367, 2003.

[36] Schuster, D., "Aerodynamic Measurements on a Large Splitter Plate for the NASA Langley Transonic Dynamics Tunnel," NASA TM 2001-210828, 2001.

[37] Dansberry, B., Durham, M., Bennett, R., Rivera, J., Silva, W., Wieseman, C., "Experimental Unsteady Pressures at Flutter on the Supercritical Wing Benchmark Model," *AIAA Structures, Structural Dynamics, and Materials Conference*, La Jolla, CA, April 19-22, 1993.